

Synchronization and exceptional points in nonreciprocal active polar mixtures

Kim L. Kreienkamp* and Sabine H. L. Klapp†

Institut für Theoretische Physik, Technische Universität Berlin

(Dated: December 2, 2024)

Many biological and synthetic active matter systems consist of different particle types that interact via nonreciprocal couplings. A striking consequence of such interactions is the spontaneous emergence of time-dependent states that break parity-time symmetry. On the field-theoretical level, the transition to these states is marked by so-called exceptional points. However, their precise impact on observable particle dynamics remains poorly understood. In this study, we address this gap by providing a scale-bridging view of a minimal active mixture with nonreciprocal polar interactions. We find that nonreciprocity induces chiral motion on the particle level, yet no full, homogeneous synchronization. Instead, we observe various behaviors, ranging from fully synchronized clusters to chimera-like states. The nonreciprocity-induced spontaneous chirality increases with the degree of nonreciprocity and peaks at coupling strengths associated with exceptional points.

I. INTRODUCTION

Nonreciprocity is ubiquitous in heterogeneous nonequilibrium systems and significantly impacts their dynamics [1–6]. Notable examples include chase-and-run behavior in bacterial predator-prey systems [7, 8] and catalytic colloids [9], robots following chiral trajectories due to opposing alignment goals [10], and demixing driven by nonreciprocal torques in mixtures of differently sized Quincke rollers [11]. More generally, nonreciprocity has shown to be crucial in neural [12, 13] and social [14, 15] networks, systems with vision cones [16–18], and quantum optics [19–23].

One particularly striking effect of nonreciprocity is its ability to induce time-dependent states [24–29]. Recently, the transition to these time-dependent states accompanied by the occurrence of exceptional points (EPs) has gained much interest [26, 27]. EPs are often discussed in the context of non-Hermitian quantum mechanics [25, 30]. For nonreciprocal systems and non-Hermitian field theories of classical systems, this framework is equally relevant. For example, in scalar nonreciprocal Cahn-Hilliard models, EPs mark the transition from a static demixed phase to a traveling demixed phase with a phase shift, which breaks PT symmetry [24, 26].

Our focus is on nonreciprocal *polar* active fluids, composed of motile particles with competing goals regarding their mutual orientation. Here, as shown by field equations [25], exceptional transitions separate regimes of (anti)flocking, i.e., coherent motion in constant direction, and chiral phases, where the polarization direction rotates over time.

In contrast, the microscopic, i.e., particle, dynamics is only partly understood. Several important questions remain: How are nonreciprocity-induced chiral states characterized on the particle level? And how does the concept of EPs, widely discussed in field theory, relate to observable particle dynamics?

To address these issues, we perform a combined continuum and particle-level analysis of a minimal model for a binary mixture of active Brownian particles [31] with additional nonreciprocal torques [25, 32–34]. The model includes both, steric repulsion and alignment couplings, each driving paradigmatic active matter transitions, namely, motility-induced phase separation [35, 36] and flocking [37–39]. The system exhibits two qualitatively distinct regimes of non-reciprocity-induced dynamics: At low intraspecies coupling strengths, nonreciprocal alignment leads to asymmetric density dynamics in which predominantly one of the two species forms clusters [33, 34]. Here, we focus on the regime of strong intraspecies coupling strengths. In this regime, the corresponding field theory predicts spontaneous time-dependent dynamics and exceptional transitions, previously associated with fully synchronized chiral phases [25]. Our particle simulations confirm that spontaneous chirality on the particle level indeed arises at sufficiently strong nonreciprocity. Yet, full synchronization involving all particles is not observed. Instead, we observe chimera-like states with a coexistence of locally synchronized and disordered regions [40]. The size of the synchronized regions and resulting polarization depends on the strength of nonreciprocity. The spontaneous chirality increases with nonreciprocity. Moreover, at coupling strengths associated with EPs the spontaneous chirality peaks.

Model.—We consider a binary mixture of circular, self-propelling particles consisting of species $a = A, B$. The particle dynamics are described by overdamped Langevin equations for the positions \mathbf{r}_i^a and the polar angles θ_i^a of the heading vectors $\mathbf{p}_i^a = (\cos \theta_i^a, \sin \theta_i^a)^T$, given by [32–34]

$$\dot{\mathbf{r}}_i^a = v_0 \mathbf{p}_i^a + \mu_r \sum_{j,b} \mathbf{F}_{\text{rep}}(\mathbf{r}_i^a, \mathbf{r}_j^b) + \sqrt{2 D_t'} \boldsymbol{\xi}_i^a \quad (1a)$$

$$\dot{\theta}_i^a = \mu_\theta \sum_{j,b \in \partial_i(R_\theta)} k_{ab} \sin(\theta_j^b - \theta_i^a) + \sqrt{2 D_r'} \eta_i^a. \quad (1b)$$

Both species have the same self-propulsion velocity (v_0) and equal mobilities (μ_r, μ_θ). The particles interact through symmetric steric repulsion (\mathbf{F}_{rep}) and are sub-

* k.kreienkamp@tu-berlin.de

† sabine.klapp@tu-berlin.de

ject to translational (ξ_i^a) and rotational (η_i^a) Gaussian white noise with zero mean and unit variance. The two species differ only in their Vicsek-like torques of strength k_{ab} . When $k_{ab} > 0$, particles of species a aim to orient parallel (align) with particles of species b within the shell ∂_i of radius R_θ . For $k_{ab} < 0$, a -particles seek to orient antiparallel (antialign) with b -particles. The interspecies couplings, k_{AB} and k_{BA} , can be either reciprocal ($k_{AB} = k_{BA}$) or nonreciprocal ($k_{AB} \neq k_{BA}$).

We set the particle diameter $\ell = \sigma$ and time $\tau = \sigma^2/D'_t$ as characteristic length and time scales. The control parameters are the particle density ρ_0^a , the reduced orientational coupling strength $g_{ab} = k_{ab} \mu_\theta \tau$, the Péclet number $Pe = v_0 \tau / \ell$, and the rotational noise strength $D_r = D'_r \tau$. For details on corresponding Brownian Dynamics (BD) simulations, see [41].

To study the impact of (non-)reciprocal torques in an otherwise symmetric system, we assume equal densities for both species, $\rho_0^A = \rho_0^B = \rho_0/2$, and equal intraspecies alignment strengths $g_{AA} = g_{BB} = g > 0$. The density ($\rho_0^a = 4/(5\pi)$), motility ($Pe = 40$), and rotational noise strength ($D_r = 3 \cdot 2^{-1/3}$) are chosen to ensure motility-induced phase separation in the absence of alignment couplings ($g_{ab} = 0 \forall ab$) [33]. The alignment radius is set to $R_\theta = 10 \ell$ (for smaller R_θ , see [41]).

The alignment couplings between particles can give rise to states with nonzero global polarization. Our system features two types of stationary polarized states: flocking (parallel orientation of A - and B -flocks) and antiflocking (antiparallel orientation) [33, 34]. In addition to these stationary polarized states, time-dependent chiral states can occur, where the polarization vector rotates over time [25]. Notably, this striking phenomenon is solely induced by nonreciprocal couplings, in the absence of any intrinsic chirality [42, 43].

Mean-field continuum analysis.—To study the emergence of chiral states, we first consider a coarse-grained description of the microscopic model (1) in terms of density fields $\rho^a(\mathbf{r}, t)$ and polarization densities $\mathbf{w}^a(\mathbf{r}, t)$ [32–34]. The full equations are given in [41]. On the continuum level, the alignment strength scales as $g'_{ab} = g_{ab} R_\theta^2 \rho_0^b / 2$. We then perform a linear stability analysis. We are mostly interested in long-wavelength (wavenumber $k = 0$) fluctuations of the polarization fields. At $k = 0$, fluctuations of the densities do not occur due to number conservation. Density fluctuations do occur at $k > 0$, but are dominated by those of the polarization at the strong coupling conditions considered here [41]. We perform linear stability analyses of the homogeneous disordered and homogeneous (anti)flocking states.

The linear stability analysis of the disordered phase (ρ^a, \mathbf{w}^a) = $(1, \mathbf{0})$ against $k = 0$ -perturbations $\sim e^{i\sigma_{\text{dis}} t}$ reveals the onset of states with non-zero polarization. The corresponding complex growth rates are given by [33]

$$\sigma_{1/2}^{\text{dis}} = g' - D_r \pm \sqrt{g'_{AB} g'_{BA}}. \quad (2)$$

Non-zero polarization emerges when $\text{Re}(\sigma_{1/2}^{\text{dis}}) > 0$. Sta-

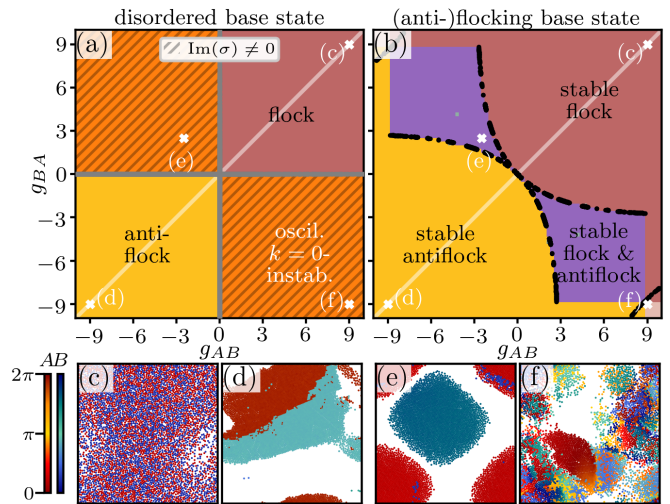


FIG. 1. Stability diagrams at $k = 0$ and particle simulation snapshots. The stability diagrams are obtained from linear stability analyses of the (a) uniform disordered and (b) homogeneous (anti)flocking base states of the continuum equations [41]. Exceptional points of the disordered and (anti)flocking base states are indicated as gray and black lines, respectively. BD simulation snapshots at (c) $g_{AB} = g_{BA} = 9$, (d) $g_{AB} = g_{BA} = -9$, (e) $g_{AB} = -g_{BA} = -2.5$, and (f) $g_{AB} = -g_{BA} = 9$. Other parameters are specified in text.

tionary flocking or antiflocking occurs when $\text{Im}(\sigma_{1/2}^{\text{dis}}) = 0$, with the associated eigenvector determining whether the system flocks or antiflocks. In contrast, $\text{Im}(\sigma_{1/2}^{\text{dis}}) \neq 0$ indicates time-dependent oscillatory polarization dynamics.

We now focus on the “strong-intraspecies-coupling” regime, where the term $g' - D_r > 0$ in Eq. (2), by setting $g = 9$. This ensures that non-zero polarization occurs regardless of the values of g_{AB} and g_{BA} . The corresponding stability diagram is shown in Fig. 1(a). Stationary flocking and antiflocking occur when both g'_{AB} and g'_{BA} are positive or negative, respectively. However, if the two species have opposing alignment goals, i.e., $g'_{AB} g'_{BA} < 0$, oscillatory polarization is predicted.

The stability of polarized states can be further analyzed by considering these as base states in a secondary linear stability analysis [41]. The result is shown in Fig. 1(b). Within the regime of opposing alignment goals there exist regions where both flocking and antiflocking are stable against $k = 0$ -perturbations [purple regimes in Fig. 1(b)]. No oscillatory instabilities emerge from (anti)flocking base states.

Exceptional points in continuum description.—The oscillatory instabilities of the disordered base states already hint at non-trivial time-dependent collective behavior in the regime of opposing alignment goals. Another indicator for time-dependent phases are so-called EPs. In the context of non-Hermitian field theories, they indicate transitions to phases with broken (generalized) PT symmetry [30], including the chiral phases found in nonrecip-

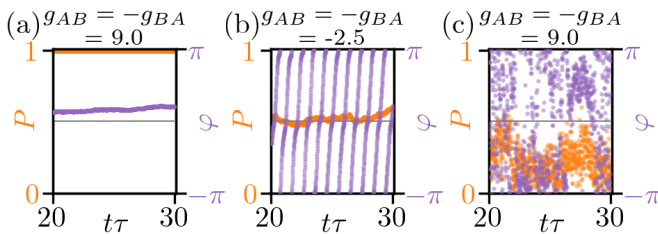


FIG. 2. Time evolution of the system-averaged polarization and phase in a single noise realization for (a) reciprocal flocking and (b,c) nonreciprocal chiral motion.

rocal polar active matter [25]. At EPs, eigenvalues of the linear stability matrix coalesce and their corresponding eigenvectors become parallel [24, 25, 27, 44]. If this happens at a bifurcation – where the system’s dynamical behavior undergoes a qualitative change – these points correspond to as “critical exceptional points” (CEPs) [28]. In the here considered system EPs (of any type) only occur for $k = 0$ -perturbations [41].

Non-critical EPs emerge from the disordered base state at the lines separating stationary (anti)flocking instabilities and oscillatory instabilities [gray lines in Figs. 1(a)].

For the (anti)flocking base states, we find (only) CEPs. They separate regimes where both flocking and antiflocking are stable from those with only stable flocking or only stable antiflocking. These CEPs are indicated as black dots in Figs. 1(b).

Particle dynamics.—We now turn to the dynamics on the particle scale. We quantify the time evolution of polarization dynamics in terms of the global polarization $P(t)$, measuring the coherence of particles, and the average phase $\varphi(t)$, defined as $P(t)e^{i\varphi(t)} = N^{-1} \sum_j^N e^{i\theta_j(t)}$ [45]. Examples for single noise realizations are shown in Fig. 2.

In reciprocal systems, sufficiently strong alignment couplings overcome noise-induced reorientation. The result is (anti)flocking, characterized by *coherent motion* of particles in constant direction [snapshots in Fig. 1(a,b)]. For $g_{AB} = g_{BA} = 9$ [Fig. 2(a)], flocking with $P(t) \approx 1$ and $\varphi(t) \approx \text{const.}$ emerges. The two species have the same single-species polarizations $P_A(t) \approx P_B(t) \approx 1$ and the same average phases $\varphi_A(t) \approx \varphi_B(t) \approx \text{const.}$ [41].

In contrast, nonreciprocal alignment can induce persistent rotational motion [25]. The phenomenon appears in all regimes with opposite alignment goals ($g_{AB}g_{BA} < 0$), yet the particle dynamics significantly depends on the degree of nonreciprocity.

To set the terminology, a *fully synchronized* phase refers to a phase where all particles of a *single* species are synchronized with $P_A \approx P_B \approx 1$. The average phases, $\varphi_A(t)$ and $\varphi_B(t)$, periodically oscillate in time. If particles of different species rotate with a constant phase shift, their motion is *phase-locked* and the combined polarization is $P(t) < 1$. In a *partially synchronized* phase, only some of the particles are synchronized, such that both $P_A, P_B < 1$. This comprises *chimera-like* phases, where

spatially separated synchronized and disordered regions coexist [40]. To quantify the rotational motion on an individual particle level, we further calculate the rate of phase differences of particles i ,

$$\Omega_s^i(t) = \frac{\theta_i(t) - \theta_i(t - \Delta t)}{\Delta t}, \quad (3)$$

where we set $\Delta t = 0.01\tau$. In the absence of any alignment couplings, the distribution $\mathcal{P}(\Omega_s^i)$ is Gaussian with zero mean and variance $2D_r/\Delta t$.

The dependence of the dynamics on nonreciprocity strength becomes clear when comparing the cases of weak and strong antisymmetric couplings, $g_{AB} = -g_{BA} = \delta$, which do *not* coincide with EPs. For weak nonreciprocity ($\delta = -2.5$), almost fully synchronized chiral motion emerges. The particles form large, rotating single-species clusters as seen in the snapshot in Fig. 1(e), and for other particle numbers in [41]. Particles in the same cluster are fully synchronized [41], while particles of different species are phase-locked [Fig. 2(b)]. The periodicity of $\varphi(t)$ reflects the continuous change of cluster polarization in *either* counterclockwise or clockwise direction. This highly periodic and synchronized rotational motion leads to the distribution $\mathcal{P}(\Omega_s^i)$ shown in Fig. 3(a). Due to synchronization, the width of $\mathcal{P}(\Omega_s^i)$ is reduced compared to the purely noise-induced Gaussian case (orange line). The mean of the distribution (black dashed line) is shifted to a non-zero value, signifying a bias towards either clockwise or counterclockwise rotation in a single noise realization. Averaging over several realizations reveals the spontaneous nature of this rotation, with equal probability for both directions, yielding zero mean chirality (not shown).

For strong nonreciprocity ($\delta = 9$), the overall collective behavior is quite different: chimera-like, partially synchronized states with smaller clusters emerge [snapshot in Fig. 1(f)]. Less synchronization and less periodic motion result in $P(t) < 0.5$ and an irregular time-dependency of $\varphi(t)$ in Fig. 2(c). Interestingly, not all particles in a single ensemble rotate in the same direction. Instead, particles rotate both clockwise and counterclockwise, balancing out the average chirality such that $\langle \Omega_s^i \rangle = 0$ [Fig. 3(c)]. The distribution itself is much wider than the noise-induced Gaussian, showing that strong nonreciprocity enhances the rotational motion of particles.

For a more complete picture of the δ -dependency of the chiral dynamics, we now focus on the ensemble-averaged *absolute value* of spontaneous chirality, $\langle |\Omega_s^i(t)| \rangle$ (ensuring that clockwise and counterclockwise rotations do not cancel out). Rotational diffusion alone leads to $\langle |\Omega_s^{\text{no align.}}| \rangle = 2\sqrt{D_r/(\pi\Delta t)} > 0$. Further we take the time- and ensemble-averaged polarization P as an indicator for the size of synchronized clusters in the system.

The polarization P and spontaneous chirality $\langle |\Omega_s^i(t)| \rangle$ are shown as functions of δ in Fig. 4. For $\delta = 0$, particles of the same species align, whereas particles of different species have no orientational couplings. This results in $P_A = P_B \approx 1$, while $P \approx 0.5$ [Fig. 4(a)].

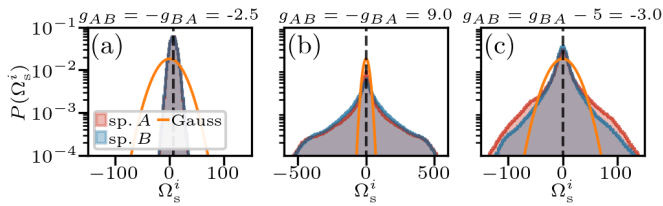


FIG. 3. Distribution $\mathcal{P}(\Omega_s^i)$ of phase difference rates in a single noise realization. The orange line indicates the Gaussian distribution induced by rotational noise alone. The black vertical dashed line indicates the average $\langle \Omega_s^i \rangle$.

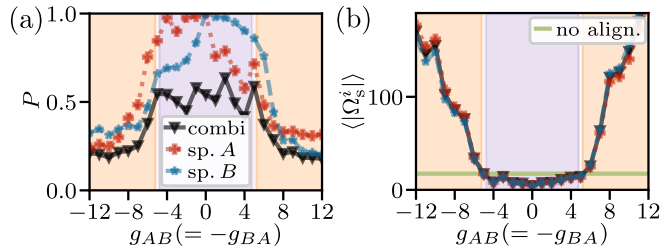


FIG. 4. Polarization and spontaneous chirality for antisymmetric system with $g_{AB} = -g_{BA} = \delta$.

Due to intraspecies alignment, which induces coherent motion of same-species particles, the absolute value of spontaneous chirality, $\langle |\Omega_s^i(t)| \rangle$, is *reduced* compared to the purely noise-induced case without any alignment [$\langle |\Omega_s^{\text{no align.}}(t)| \rangle$, green line in Fig. 4(b)].

The behavior for small $|\delta| \lesssim 5$ (purple-shaded areas in Fig. 4) is qualitatively the same we already discussed for $\delta = -2.5$. Here, nonreciprocal interspecies interactions are relatively weak compared to intraspecies alignment. The combined polarization remains around $P \approx 0.5$ and the spontaneous chirality remains lower than $\langle |\Omega_s^{\text{no align.}}(t)| \rangle$. Interestingly, the spontaneous chirality is nearly the same for both species, while the polarization differs. For $\delta > (<)0$, $B(A)$ -particles remain synchronized [$P_{B(A)} \approx 1$ in Fig. 4(a)]. Yet, by trapping particles of the other species inside their cluster as seen in Fig. 1(e), they inhibit full synchronization of the latter ($P_{A(B)} < 1$).

When nonreciprocity becomes stronger ($|\delta| \gtrsim 5$, orange-shaded area in Fig. 4), the overall polarization P gradually decreases and the spontaneous chirality increases. In this regime, nonreciprocity-induced spontaneous chirality dominates over alignment-induced coherent motion. Partially synchronized, chimera-like states emerge as exemplarily discussed above for $\delta = 9$ [Figs. 2(c),3(b)].

For even stronger nonreciprocity [$|\delta| \geq 9$, Fig. 1(f)], additional asymmetric clustering leads to $P_{B(A)} < P_{A(B)}$ for $\delta > (<)0$ [33, 34]. These effects are also reflected in the orientational correlation functions [41]. In systems with nonrepulsive particles, the spontaneous chirality is even enhanced, implying that steric interactions perturb chirality [41].

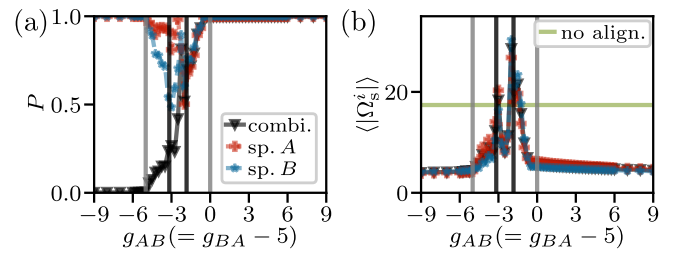


FIG. 5. Polarization and spontaneous chirality for antisymmetric system with $g_{AB} = g_{BA} - 5$. The vertical gray and black lines indicate non-critical and critical exceptional points, respectively.

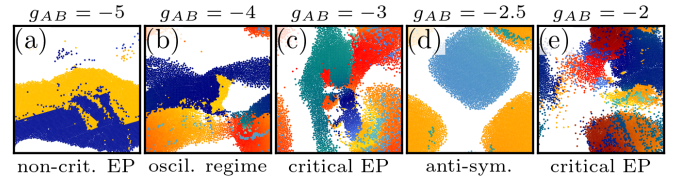


FIG. 6. Snapshot of BD simulations in the vicinity of exceptional points with $g_{BA} = g_{AB} + 5$. Particle species and orientation are denoted in the same colors as in Fig. 1.

Signature of exceptional points in particle description—We now turn to the *transition* to the chiral phase and the signatures of EPs in particle dynamics. To this end, we consider nonreciprocal systems with $g_{AB} = g_{BA} - d$, where $d \neq 0$ is fixed. By varying g_{AB} , we cross non-critical EPs of the disordered base state twice and CEPs of the antiflocking and flocking base states once each.

In Fig. 5 we present the time- and ensemble-averaged polarization and spontaneous chirality along the line $g_{AB} = g_{BA} - 5$ in Fig. 1(a,b). As g_{AB} moves from negative to positive, the system goes from antiflocking ($P \approx 0$) to flocking ($P \approx 1$), both characterized by coherent motion and, consequently, small $\langle |\Omega_s^i| \rangle$. Between these states, separated by non-critical EPs, lies the regime of oscillatory $k = 0$ -instabilities, where P gradually increases from 0 and 1. The spontaneous chirality begins to increase once the system crosses the non-critical EPs, indicating enhanced particle rotation inside the oscillatory instability regime [Fig. 5(b)]. Strikingly, we observe peaks of this quantity at the coupling values related to CEPs. This increase is accompanied by high values of susceptibility $\chi = N \text{Var}(P)$ [41].

As an illustration, we show snapshots of particle simulations close to EPs in Fig. 6. At the non-critical EP ($g_{AB} = -5$), antiflocking still persists [Fig. 6(a)]. Within the oscillatory regime [$g_{AB} = -4$, Fig. 6(b)], synchronization of same-species particles is already reduced. At the CEPs [$g_{AB} = -3$ and $g_{AB} = -2$ in Figs. 6(c,e)], clusters dynamically form and break up. The synchronization is further reduced and particles rotate in both clockwise and counterclockwise directions, yielding a broad frequency distribution, as shown in Fig. 3(c). This CEP-

related behavior contrasts with the one in-between the CEPs ($g_{AB} = -2.5$), characterized by large, synchronized single-species clusters and a narrow frequency distribution [Figs. 6(d),3(a)].

Conclusion—We demonstrate that nonreciprocal orientational couplings induce spontaneous chirality and synchronization in particle systems for a broad range of parameters. The coherence of chiral motion depends crucially on the strength of nonreciprocity. In particular, critical exceptional points, indicating the transition to time-dependent states on a mean-field level, leave clear signatures on the microscopic scale: in their vicinity, the nonreciprocity-induced chirality peaks and markedly exceeds values in fully antisymmetric systems. Our study constitutes a scale-bridging view on the effects of nonreciprocity on observable particle dynamics. Notably, nonreciprocity-induced chirality is also observed in the absence of repulsion, across different system sizes, and for various coupling radii.

The chiral states in our polar active fluid are persistent on the timescale of the simulation. This is in stark contrast to the two-dimensional Ising lattice model, where nonreciprocity destabilizes static and time-dependent ordering of spins [29, 46]. Further work is necessary to understand the long-time stability in different interacting nonreciprocal systems, as well as their thermodynamic consequences [27, 28, 47], on the microscopic level. Our results could be tested experimentally, for instance, using robotic systems [10] or optically coupled nanoparticles [22, 23].

ACKNOWLEDGMENTS

This work was funded by the Deutsche Forschungsgemeinschaft (DFG, German Research Foundation) – Projektnummer 163436311 (SFB 910) and Projektnummer 517665044.

-
- [1] A. V. Ivlev, J. Bartnick, M. Heinen, C.-R. Du, V. Nosenko, and H. Löwen, *Phys. Rev. X* **5**, 011035 (2015).
 - [2] C. H. Meredith, P. G. Moerman, J. Groenewold, Y.-J. Chiu, W. K. Kegel, A. van Blaaderen, and L. D. Zarzar, *Nat. Chem.* **12**, 1136 (2020).
 - [3] S. Saha, J. Agudo-Canalejo, and R. Golestanian, *Phys. Rev. X* **10**, 041009 (2020).
 - [4] T. Frohoff-Hülsmann and U. Thiele, *Phys. Rev. Lett.* **131**, 107201 (2023).
 - [5] M. Fruchart, C. Scheibner, and V. Vitelli, *Annu. Rev. Condens. Matter Phys.* **14**, 471 (2023).
 - [6] R. Mandal, S. S. Jaramillo, and P. Sollich, *Phys. Rev. E* **109**, L062602 (2024).
 - [7] L. Xiong, Y. Cao, R. Cooper, W.-J. Rappel, J. Hasty, and L. Tsimring, *eLife* **9**, e48885 (2020).
 - [8] E. Theveneau, B. Steventon, E. Scarpa, S. Garcia, X. Trepát, A. Streit, and R. Mayor, *Nat. Cell Biol.* **15**, 763 (2013).
 - [9] S. Saha, S. Ramaswamy, and R. Golestanian, *New J. Phys.* **21**, 063006 (2019).
 - [10] J. Chen, X. Lei, Y. Xiang, M. Duan, X. Peng, and H. Zhang, *Phys. Rev. Lett.* **132**, 118301 (2024).
 - [11] S. Maity and A. Morin, *Phys. Rev. Lett.* **131**, 178304 (2023).
 - [12] H. Sompolinsky and I. Kanter, *Phys. Rev. Lett.* **57**, 2861 (1986).
 - [13] H. Rieger, M. Schreckenberg, and J. Zittartz, *Zeitschrift für Physik B Condensed Matter* **74**, 527 (1989).
 - [14] H. Hong and S. H. Strogatz, *Phys. Rev. Lett.* **106**, 054102 (2011).
 - [15] D. Helbing and P. Molnár, *Phys. Rev. E* **51**, 4282 (1995).
 - [16] L. Barberis and F. Peruani, *Phys. Rev. Lett.* **117**, 248001 (2016).
 - [17] F. A. Lavergne, H. Wendehenne, T. Bäuerle, and C. Bechinger, *Science* **364**, 70 (2019).
 - [18] S. A. Loos, S. H. Klapp, and T. Martynek, *Phys. Rev. Lett.* **130**, 198301 (2023).
 - [19] A. Metelmann and A. A. Clerk, *Phys. Rev. X* **5**, 021025 (2015).
 - [20] S. Zhang, Y. Hu, G. Lin, Y. Niu, K. Xia, J. Gong, and S. Gong, *Nat. Photonics* **12**, 744 (2018).
 - [21] A. McDonald, R. Hanai, and A. A. Clerk, *Phys. Rev. B* **105**, 064302 (2022).
 - [22] M. Reisenbauer, H. Rudolph, L. Egyed, K. Hornberger, A. V. Zasedatelev, M. Abuzarli, B. A. Stickler, and U. Delić, *Nat. Phys.* **20**, 1629 (2024).
 - [23] V. Liška, T. Zemánková, P. Jákł, M. Šiler, S. H. Simpson, P. Zemánek, and O. Brzobohatý, *Nat. Phys.* **20**, 1622 (2024).
 - [24] Z. You, A. Baskaran, and M. C. Marchetti, *Proc. Natl. Acad. Sci. U.S.A.* **117**, 19767 (2020).
 - [25] M. Fruchart, R. Hanai, P. B. Littlewood, and V. Vitelli, *Nature* **592**, 363 (2021).
 - [26] T. Suchanek, K. Kroy, and S. A. M. Loos, *Phys. Rev. Lett.* **131**, 258302 (2023).
 - [27] T. Suchanek, K. Kroy, and S. A. M. Loos, *Phys. Rev. E* **108**, 064123 (2023).
 - [28] T. Suchanek, K. Kroy, and S. A. Loos, *Phys. Rev. E* **108**, 064610 (2023).
 - [29] Y. Avni, M. Fruchart, D. Martin, D. Seara, and V. Vitelli, *arXiv preprint arXiv:2311.05471* (2023).
 - [30] M.-A. Miri and A. Alu, *Science* **363**, eaar7709 (2019).
 - [31] P. Romanczuk, M. Bär, W. Ebeling, B. Lindner, and L. Schimansky-Geier, *Eur. Phys. J.: Spec. Top.* **202**, 1 (2012).
 - [32] K. L. Kreienkamp and S. H. L. Klapp, *New J. Phys.* **24**, 123009 (2022).
 - [33] K. L. Kreienkamp and S. H. L. Klapp, *arXiv preprint arXiv:2403.19291* (To appear in *Phys. Rev. Lett.*) (2024).
 - [34] K. L. Kreienkamp and S. H. L. Klapp, *arXiv preprint arXiv:2404.06305* (To appear in *Phys. Rev. E*) (2024).
 - [35] M. E. Cates and J. Tailleur, *Annu. Rev. Condens. Matter Phys.* **6**, 219 (2015).
 - [36] J. Bialké, H. Löwen, and T. Speck, *EPL* **103**, 30008 (2013).

- [37] M. C. Marchetti, J.-F. Joanny, S. Ramaswamy, T. B. Liverpool, J. Prost, M. Rao, and R. A. Simha, *Rev. Mod. Phys.* **85**, 1143 (2013).
- [38] T. Vicsek, A. Czirók, E. Ben-Jacob, I. Cohen, and O. Shochet, *Phys. Rev. Lett.* **75**, 1226 (1995).
- [39] G. Grégoire and H. Chaté, *Phys. Rev. Lett.* **92**, 025702 (2004).
- [40] D. M. Abrams and S. H. Strogatz, *Phys. Rev. Lett.* **93**, 174102 (2004).
- [41] See Supplemental Material at [url] for additional information about our models and details on our methods of analysis.
- [42] B. Liebchen and D. Levis, *Phys. Rev. Lett.* **119**, 058002 (2017).
- [43] D. Levis and B. Liebchen, *J. Condens. Matter Phys.* **30**, 084001 (2018).
- [44] R. El-Ganainy, K. G. Makris, M. Khajavikhan, Z. H. Musslimani, S. Rotter, and D. N. Christodoulides, *Nat. Phys.* **14**, 11 (2018).
- [45] J. A. Acebrón, L. L. Bonilla, C. J. Pérez Vicente, F. Ritort, and R. Spigler, *Rev. Mod. Phys.* **77**, 137 (2005).
- [46] Y. Avni, M. Fruchart, D. Martin, D. Seara, and V. Vitelli, arXiv preprint arXiv:2409.07481 (2024).
- [47] S. A. M. Loos and S. H. L. Klapp, *New J. Phys.* **22**, 123051 (2020).

Supplemental Material to “Synchronization and exceptional points in nonreciprocal active polar mixtures”

Kim L. Kreienkamp* and Sabine H. L. Klapp†
Institut für Theoretische Physik, Technische Universität Berlin

In this supplemental, we provide further details to support the analysis and findings on nonreciprocity-induced spontaneous chirality in nonreciprocal polar active matter. For the particle-level analysis, we examine finite-size effects and present supplementary results on the susceptibility and orientational correlations functions. At the continuum level, we include the complete field equations and perform a detailed linear stability analysis of polarized states, addressing arbitrary wavenumbers. To demonstrate the impact of nonreciprocal alignment for a broader range of systems, we present both particle- and continuum-level results for a smaller alignment radius than considered in the main text and, finally, discuss the influence of repulsive interactions from a particle-level perspective.

CONTENTS

| | |
|---|----|
| I. Microscopic model | 1 |
| A. Finite-size effects | 2 |
| II. Particle-simulation results | 3 |
| A. Polarization and average phase of each species | 3 |
| B. Susceptibilities | 4 |
| C. Orientational correlation functions | 5 |
| III. Continuum model | 5 |
| A. Continuum equations | 5 |
| B. Infinite-wavelength limit | 6 |
| C. Parameter choice | 6 |
| IV. Field-theoretical results | 6 |
| A. Mean-field linear stability analysis around (anti)flocking base states | 6 |
| B. Characterization of emerging states | 8 |
| C. Exceptional points | 9 |
| D. Results for finite-wavelength perturbations | 9 |
| V. Smaller alignment radius: continuum versus particle scale | 10 |
| VI. Effect of repulsion on the particle scale | 12 |
| VII. List of supplementary videos | 12 |
| References | 13 |

I. MICROSCOPIC MODEL

On a microscopic level, the motion of particles is governed by the Langevin Eqs. (1a) and (1b) in the main text. The translational Langevin Eq. (1a) captures the hard-sphere nature of the particles via the repulsive force $\mathbf{F}_{\text{rep}}(\mathbf{r}_i^a, \mathbf{r}_j^b) = -\sum_{(b,j) \neq (a,i)} \nabla_{a,i} U(r_{ij}^{ab})$, where $U(r_{ij}^{ab})$ is the Weeks-Chandler-Andersen potential [1]

$$U(r_{ij}^{ab}) = \begin{cases} 4\epsilon \left[\left(\frac{\sigma}{r_{ij}^{ab}} \right)^{12} - \left(\frac{\sigma}{r_{ij}^{ab}} \right)^6 + \frac{1}{4} \right], & \text{if } r_{ij}^{ab} < r_c \\ 0, & \text{else} \end{cases}, \quad (1)$$

* k.kreienkamp@tu-berlin.de

† sabine.klapp@tu-berlin.de

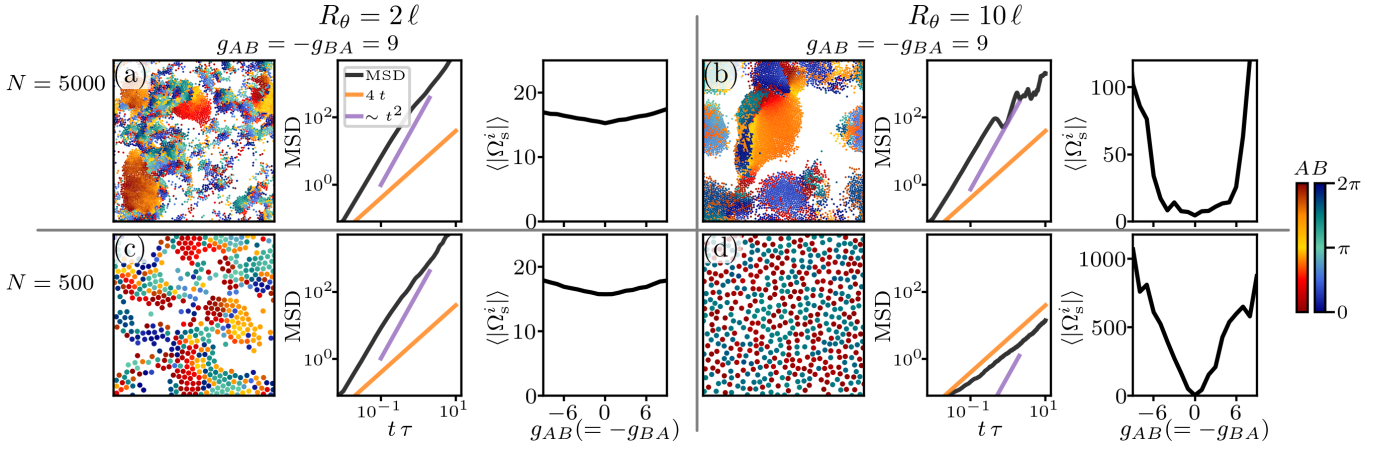


FIG. 1. Mean-squared displacement (MSD), spontaneous chirality and snapshots for antisymmetric systems of different size and interaction radius. The snapshots and MSDs are shown for $g_{AB} = -g_{BA} = 9$. (a) $N = 5000$ particles, $R_\theta = 2\ell$. (b) $N = 5000$ particles, $R_\theta = 10\ell$. (c) $N = 500$ particles, $R_\theta = 2\ell$. (d) $N = 500$ particles, $R_\theta = 10\ell$. The simulation box length is $L = 99\ell$ for $N = 5000$ and $L_{500} = 31.3\ell$ for $N = 500$. The MSD is defined as $\text{MSD} = \langle (\mathbf{r}(t) - \mathbf{r}(0))^2 \rangle \ell^2$.

where $r_{ij}^{ab} = |\mathbf{r}_{ij}^{ab}| = |\mathbf{r}_i^a - \mathbf{r}_j^b|$. The cut-off distance is $r_c = 2^{1/6} \sigma$ with particle diameter σ as characteristic length scale, $\ell = \sigma = 1$. The characteristic energy scale is $\epsilon = \epsilon^* k_B T$, where k_B is the Boltzmann's constant and T is the temperature. We set the thermal energy to the energy unit, i.e., $k_B T = 1$. The characteristic time scale $\tau = \sigma^2/D_t' = 1$ is the time required for a passive particles to travel its own diameter.

Particle positions and orientations are influenced by thermal noise. The Gaussian white noise processes $\xi_i^a(t)$ and $\eta_i^a(t)$ have zero mean and delta-correlated variances $\langle \xi_{i,k}^a(t) \xi_{j,l}^b(t') \rangle = \delta_{ij} \delta_{ab} \delta_{kl} \delta(t - t')$ and $\langle \eta_i^a(t) \eta_j^b(t') \rangle = \delta_{ij} \delta_{ab} \delta(t - t')$. The mobilities μ_r and μ_θ are related to thermal noise via $\mu_r = D_t'/(k_B T)$ and $\mu_\theta = D_r'/(k_B T)$.

We perform numerical Brownian Dynamics (BD) simulations of the Langevin Eqs. (1a) and (1b) in the main text in an $L \times L$ box with periodic boundary conditions. The dimensionless simulation parameters are chosen as following. The overall area fraction is set to $\Phi = (\rho_0^A + \rho_0^B) \pi \ell^2/4 = 0.4$ with number density $\rho_0^a = N_a/L$. The number of particles of each species is equal, i.e., $\Phi_A = \Phi_B = \Phi/2$. The Péclet number is set to $\text{Pe} = 40$ and the repulsive strength to $\epsilon^* = 100$. The diffusion constants are $D_t' = 1 \ell^2/\tau$ and $D_r' = 3 \cdot 2^{-1/3}/\tau$. The dimensionless orientational coupling strengths are $g_{ab} = k_{ab} \mu_\theta \tau$. Focusing on strong intraspecies couplings, we set $g_{AA} = g_{BB} = 9$, while g_{AB} , g_{BA} are chosen independently. In all simulations in the main text, the cut-off radius for orientational couplings is set to $R_\theta = 10\ell$ with a total of $N = 5000$ particles. The system is initialized in a random configuration. We use an Euler-Mayurama algorithm to integrate the equations of motion with a timestep of $\delta t = 10^{-5} \tau$. We let the simulations reach a steady state before data evaluation.

A. Finite-size effects

The results presented in the main text are based on simulations with $N = 5000$ particles of diameter $\ell = \sigma$ at a fixed area fraction of $\Phi = 0.4$. This corresponds to a simulation box length of $L = 99\ell$. The orientational coupling radius considered in the main text is $R_\theta = 10\ell$. In the following, we address potential finite-size effects due to an interplay between L and R_θ . (The interplay between R_θ and short-range repulsion is discussed separately in Sec. VI.)

To study the role of finite-size effects, we first qualitatively compare simulation results for two different system sizes ($N = 500$ with $L_{500} = 31.3\ell$ and $N = 5000$ with $L = 99\ell$) and two different coupling radii ($R_\theta = 2\ell$ and $R_\theta = 10\ell$). To this end, we present in Fig. 1 simulation snapshots and mean-squared displacements (MSDs) for $g_{AB} = -g_{BA} = 9$, and spontaneous chiralities as functions of the antisymmetric coupling strength $g_{AB} = -g_{BA}$. The MSD, defined as $\langle (\mathbf{r}(t) - \mathbf{r}(0))^2 \rangle \ell^2$, quantifies the translational motion by measuring particle displacements over time. This enables differentiation between dynamical and frozen states (where particle positions are essentially fixed).

When $R_\theta \ll L$, i.e., for $N = 5000$ with (a) $R_\theta = 2\ell$ or (b) $R_\theta = 10\ell$, and (c) $N = 500$ with $R_\theta = 2\ell$, particles form clusters, with a preference for pure A -species clusters. This nonreciprocity-induced asymmetric clustering has been described in detail in [2, 3]. As seen from the similarity of the MSDs for $R_\theta = 2\ell$ and $R_\theta = 10\ell$ in systems with $N = 5000$ particles [Figs. 1(a,b)], the larger interaction radius of $R_\theta = 10\ell$ does not significantly impact the asymmetric clustering of particles. The values of spontaneous chirality, on the other hand, increase with increasing alignment radius (and, thus, increasing effective coupling strength), see Sec. V.

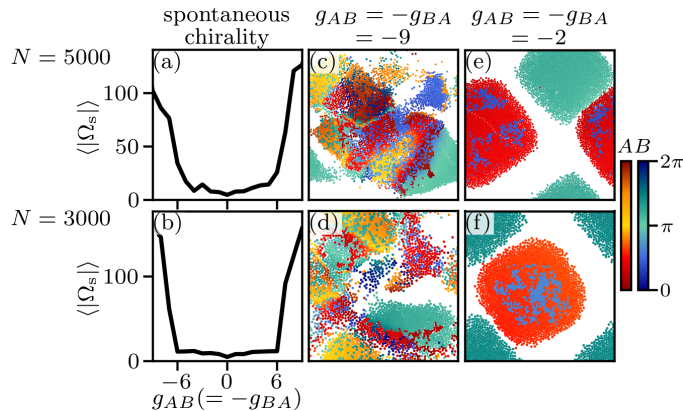


FIG. 2. Comparison of nonreciprocity-induced chirality for systems with different numbers of particles. Spontaneous chirality as a function of antisymmetric couplings $g_{AB}(= -g_{BA})$ for (a) $N = 5000$ and (b) $N = 3000$ particles. Simulation snapshots for $g_{AB} = -g_{BA} = -9$ with (c) $N = 5000$ and (d) $N = 3000$ and for $g_{AB} = -g_{BA} = -2$ with (e) $N = 5000$ and (f) $N = 3000$. The alignment radius is $R_\theta = 10\ell$. The simulation box lengths are $L = 99\ell$ for $N = 5000$ and $L_{3000} = 77\ell$ for $N = 3000$ particles.

However, when the alignment radius becomes comparable to the simulation box size, the qualitative behavior changes significantly. This is demonstrated for systems with $R_\theta = 10\ell$ and $N = 500$ particles, where $L_{500} = 31.3\ell$, see Figs. 1(d). From the snapshot, we see that particles are now homogeneously distributed throughout the system without forming any clusters. The corresponding MSD clearly indicates subdiffusive behavior. The spontaneous chirality in these systems is an order of magnitude larger than for $N = 5000$. The drastic change in dynamical behavior can be attributed to finite-size effects, which are absent for the results in larger systems presented in the main text. Interestingly, this fully synchronized, “frozen” state with essentially homogeneous particle distribution resembles the absorbing state seen in nonreciprocal robot experiments [4].

To confirm that finite-size effects do not affect the qualitative dynamics of the system considered in the main text (with $N = 5000$ and $R_\theta = 10\ell$), we compare results for $N = 5000$ and $N = 3000$ particles in Fig. 2. The spontaneous chirality as a function of antisymmetric couplings $g_{AB}(= -g_{BA})$ is shown in Figs. 2(a,b) for $N = 5000$ and $N = 3000$, respectively. For both system sizes, the spontaneous chirality is small and nearly constant for moderate nonreciprocity and increases (quickly) at higher values of nonreciprocity. While the magnitude of spontaneous chirality is larger in the $N = 3000$ system, the order of magnitude remains the same. Importantly, the snapshots in Figs. 2(c-f) show that the qualitative behavior is the same for both system sizes: Asymmetric, less synchronized clusters form for strong nonreciprocity [$g_{AB} = -g_{BA} = -9$, Figs. 2(c,d)], while large synchronized clusters of both species emerge for weaker nonreciprocity [$g_{AB} = -g_{BA} = -2$, Figs. 2(e,f)].

These findings confirm that the results for $N = 5000$ in the main text are not significantly influenced by finite-size effects.

II. PARTICLE-SIMULATION RESULTS

In this section, we provide additional particle simulation results for the parameters given in Sec. I.

A. Polarization and average phase of each species

In the main text we have focused on the characteristic time evolutions of the combined polarization, $P(t)$, and average phase, $\varphi(t)$, of *all* particles (Fig. 2 in main text).

The time evolutions of the *single-species* polarizations and average phases are shown in Fig. 3. For the reciprocal flocking case with $g_{AB} = g_{BA} = 9$, coherent motion with $P_B(t) = P_A(t) = 1$ and $\varphi_A(t) = \varphi_B(t) \approx \text{const.}$ emerges [Fig. 3(a)]. For weak-reciprocity ($g_{AB} = -g_{BA} = -2.5$), particles of the same species (nearly) fully synchronize, such that $P_A \approx P_B \approx 1$ [Fig. 3(b)]. The average phases, $\varphi_A(t)$ and $\varphi_B(t)$, of both species oscillate periodically in time, yet with a phase-shift. This corresponds to phase-locked, full synchronization of *A*- and *B*-particles. At larger nonreciprocity ($g_{AB} = -g_{BA} = 9$), partial synchronization emerges [Fig. 3(c)]. The single species polarizations are $0 < P_A, P_B < 1$, reflecting the synchronization of some but not all particles. The average phase changes aperiodically in time.

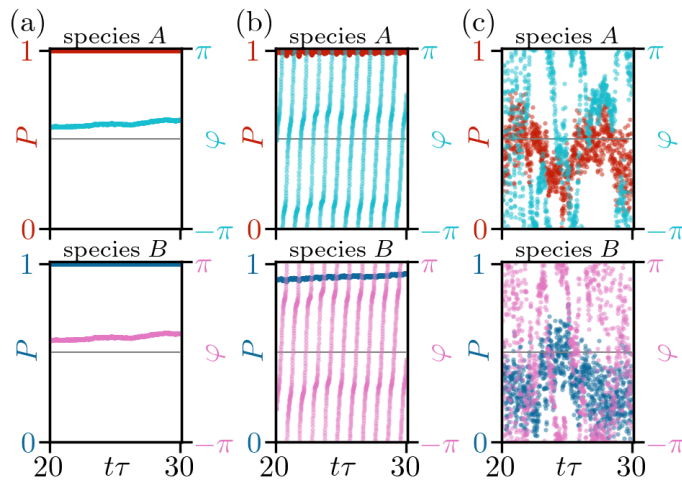


FIG. 3. Polarization and average phase of particles of a single over time for (a) reciprocal flocking with $g_{AB} = g_{BA} = 9$ and nonreciprocal chiral motion with (b) $g_{AB} = -g_{BA} = -2.5$ and (c) $g_{AB} = -g_{BA} = 9$.

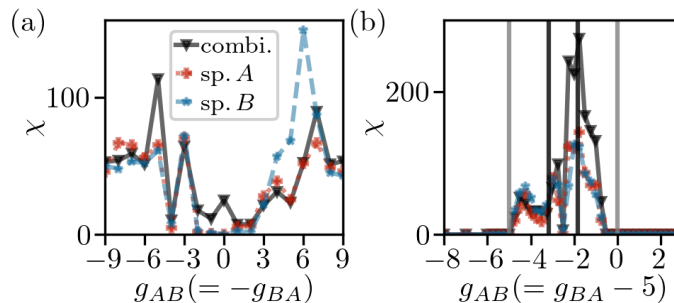


FIG. 4. Susceptibility for (a) $g_{AB} = -g_{BA}$ and (b) $g_{AB} = g_{BA} - 5$. Exceptional points of the disordered and (anti)flocking base states are marked as gray and black vertical lines, respectively. The alignment interaction radius is $R_\theta = 10\ell$. Other parameters are specified in Sec. I.

B. Susceptibilities

The susceptibility $\chi = N \text{Var}(P)$ measures polarization fluctuations in the system. It can be determined as

$$\chi(P) = \frac{1}{N} \left(\left\langle \left\| \sum_{i=1}^N \mathbf{p}_i \right\| \left\| \sum_{j=1}^N \mathbf{p}_j \right\| \right\rangle - \left\langle \left\| \sum_{i=1}^N \mathbf{p}_i \right\|^2 \right\rangle \right) \quad (2)$$

from individual particle orientation vectors $\mathbf{p}_i = (\cos(\theta_i), \sin(\theta_i))^T$. Near flocking transitions, the susceptibility typically peaks [3, 5]. In the strong-coupling regime considered here, stationary (anti)flocking or oscillatory $k = 0$ -instabilities occur for all interspecies couplings. This means there is no “standard” flocking transition from a disordered to an ordered state.

In antisymmetric systems with $g_{AB} = -g_{BA} = \delta \neq 0$, the continuum theory predicts oscillatory $k = 0$ -instabilities, without crossing any exceptional points. In this case, the susceptibility calculated from BD simulations increases with the strength of nonreciprocity, $|\delta|$, as shown in Fig. 4(a).

For $g_{AB} = g_{BA} - d$ (with fixed $d \neq 0$), exceptional points of both the disordered and (anti)flocking base states are crossed upon varying g_{AB} . As shown in Fig. 4(b), the susceptibility is zero outside and non-zero within the regime of oscillatory instabilities, marked by the gray vertical lines. Interestingly, the susceptibility is largest between the critical exceptional points of the flocking and antiflocking states, indicated by the black vertical lines.

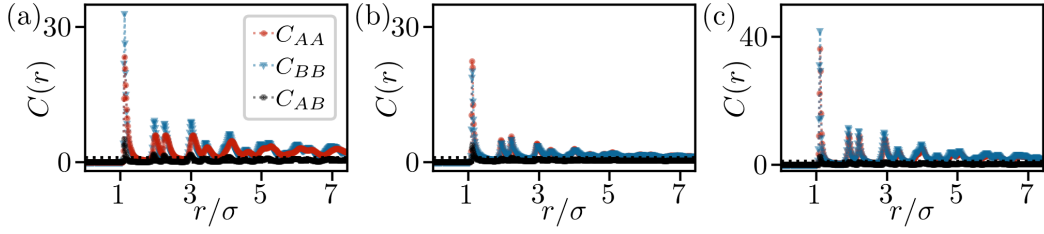


FIG. 5. Orientational correlation function for the antisymmetric cases (a) $g_{AB} = -g_{BA} = 2$ and (b) $g_{AB} = -g_{BA} = 9$, and close to the exceptional point (c) $g_{AB} = g_{BA} - 5 = -3$.

C. Orientational correlation functions

Here we comment on the orientational spatial structure in systems with fully antisymmetric couplings $g_{AB} = -g_{BA}$ and close to exceptional points. These can be analyzed in terms of the orientational correlation function [3, 6]

$$C_{ab}(r) = \frac{1}{\mathcal{N}} \sum_i^{N_a} \sum_j^{N_b} \mathbf{p}_i^a \cdot \mathbf{p}_j^b \delta(r - |\mathbf{r}_i^a - \mathbf{r}_j^b|), \quad (3)$$

where $\mathcal{N} = N_a N_b 4\pi r^2/V$ and $\mathbf{p}_i^a, \mathbf{p}_j^b$ denote the orientation vectors of particles i and j of species a and b , respectively. In nonreciprocal mixtures, the single-species correlations generally differ, i.e., $C_{AA} \neq C_{BB}$ [3, 7]. The orientational correlation functions $C_{ab}(r)$ are shown in Fig. 5 for different strengths of nonreciprocity.

For moderate nonreciprocity ($0 < \delta < 9$), the polarization of the species B is generally larger compared to those of the species A [Fig. 4(a) in main text]. Then, for $g_{AB} = -g_{BA} = \delta = 2$, the stronger synchronization of B particles is reflected by $C_{BB} \geq C_{AA}$ [Fig. 5(a)]. As nonreciprocity increases, the correlation range of particle orientations decreases, see Fig. 5(b). For $\delta = 9$, asymmetric A -clustering leads to $C_{AA} \geq C_{BB}$ [2, 3]. The orientational correlations C_{AB} between different particle species are generally weak.

Finally, the orientational correlation function close to a critical exceptional point, $g_{AB} = g_{BA} - 5 = -3$, is shown in Fig. 5(c). For small distances $r \leq 3\sigma$, the magnitude of $C(r)$ is enhanced compared to the case of moderate nonreciprocity [Fig. 5(a)].

III. CONTINUUM MODEL

A. Continuum equations

The continuum equations are derived from the microscopic Langevin Eqs. (1a) and (1b) given the main text as outlined in [2, 3, 8]. The evolution equation for the density field $\rho^a = \rho^a(\mathbf{r}, t)$ of species a is given as

$$\partial_t \rho^a + \nabla \cdot \mathbf{j}_a = 0 \quad (4)$$

with flux

$$\mathbf{j}_a = v^{\text{eff}}(\rho) \mathbf{w}^a - D_t \nabla \rho^a. \quad (5)$$

The polarization density $\mathbf{w}^a = \mathbf{w}^a(\mathbf{r}, t)$ evolves like

$$\begin{aligned} \partial_t \mathbf{w}^a = & -\frac{1}{2} \nabla (v^{\text{eff}}(\rho) \rho^a) - D_r \mathbf{w}^a + \sum_b g'_{ab} \rho^a \mathbf{w}^b + D_t \nabla^2 \mathbf{w}^a + \frac{v^{\text{eff}}(\rho)}{16 D_r} \nabla^2 (v^{\text{eff}}(\rho) \mathbf{w}^a) - \sum_{b,c} \frac{g'_{ab} g'_{ac}}{2 D_r} \mathbf{w}^a (\mathbf{w}^b \cdot \mathbf{w}^c) \\ & - \frac{z}{16 D_r} \nabla \rho \cdot [\nabla (v^{\text{eff}}(\rho) \mathbf{w}^a) - \nabla^* (v^{\text{eff}}(\rho) \mathbf{w}^{a*})] + \sum_b \frac{g'_{ab}}{8 D_r} \left[\mathbf{w}^b \cdot \nabla (v^{\text{eff}}(\rho) \mathbf{w}^a) + \mathbf{w}^{b*} \cdot \nabla (v^{\text{eff}}(\rho) \mathbf{w}^{a*}) \right. \\ & \left. - 2 \left\{ v^{\text{eff}}(\rho) \mathbf{w}^a \cdot \nabla \mathbf{w}^b + \mathbf{w}^b \nabla \cdot (v^{\text{eff}}(\rho) \mathbf{w}^a) - v^{\text{eff}}(\rho) \mathbf{w}^{a*} \cdot \nabla \mathbf{w}^{b*} - \mathbf{w}^{b*} \nabla \cdot (v^{\text{eff}}(\rho) \mathbf{w}^{a*}) \right\} \right], \end{aligned} \quad (6)$$

where $\mathbf{w}^* = (w_y, -w_x)^T$ and $\nabla^* = (\partial_y, -\partial_x)^T$. As explained in [2, 3, 8], the continuity Eq. (4) for the particle densities describe that the motion of particles results from self-propulsion in direction \mathbf{w}^a and translational diffusion of strength D_t . Importantly, the self-propulsion velocity is not constant but depends on the density like $v^{\text{eff}}(\rho) = \text{Pe} - z\rho$ with

$\rho = \sum_b \rho^b$. The density-dependent velocity models the effect of steric repulsion, as it reflects the slowing down of particles in crowded situations, where free motion is hindered by others. The main contributions to the evolution of polarization densities [Eq. (6)] are the drift of particles towards low-density regions (first term on right-hand side), the decay of polarization induced by rotational diffusion (second term), and the orientational couplings between particles of all species (third term). The other contributions are of diffusional origin or non-linear, smoothing out low- and high-polarization regimes.

The continuum equations are non-dimensionalized with characteristic time (τ) and length (ℓ) scales. Furthermore, ρ^a and \mathbf{w}^a are scaled with the average particle density ρ_0^a . The control parameters are the Péclet number $\text{Pe} = v_0 \tau / \ell$, the velocity-reduction parameter $z = \zeta \rho_0^a \tau / \ell$, the translational diffusion coefficient $D_t = \xi \tau / \ell^2$, the rotational diffusion coefficient $D_r = \eta \tau$, and the relative orientational coupling parameter $g'_{ab} = k_{ab} \mu_\theta R_\theta^2 \rho_0^b \tau / 2$. Note that g'_{ab} scales with the average density ρ^b and the alignment radius R_θ^2 .

B. Infinite-wavelength limit

We are mainly interested in $k = 0$ -fluctuations of the polarization fields. These can be studied in a mean-field approximation of the full model (4)-(6) by neglecting all gradient terms. The mean-field ($k = 0$ -)polarization dynamics is given by [2, 9]

$$\partial_t \begin{pmatrix} \mathbf{w}^A \\ \mathbf{w}^B \end{pmatrix} = \begin{pmatrix} g' - D_r - \frac{\mathcal{Q}_A^2}{2D_r} & g'_{AB} \\ g'_{BA} & g' - D_r - \frac{\mathcal{Q}_B^2}{2D_r} \end{pmatrix} \cdot \begin{pmatrix} \mathbf{w}^A \\ \mathbf{w}^B \end{pmatrix} \quad (7)$$

with

$$\mathcal{Q}_a = g' \mathbf{w}^a + g'_{ab} \mathbf{w}^b \text{ with } b \neq a. \quad (8)$$

Note that density fields are constant because they are conserved.

C. Parameter choice

Most parameters of the continuum model can be directly adopted from the considered particle simulation parameters. We use the same Péclet number, $\text{Pe} = 40$, and the same rotational diffusion constant, $D_r = \eta \tau = 3 \cdot 2^{-1/3}$. The number density $\rho_0 = 2 \rho_0^a = 4/\pi \Phi$, where $\rho_0^a = 2/\pi \Phi$, is obtained from the area fraction $\Phi = 0.4$ in particle simulations. For the alignment radius $R_\theta = 10 \ell$ considered in the main text, the orientational coupling strengths on the continuum level (g'_{ab}) are related to those in the particle simulations (g_{ab}) via $g'_{ab} = 12.73 g_{ab}$. When we compare our results to the case with smaller $R_\theta = 2 \ell$, $g'_{ab} = 0.51 g_{ab}$. In this study, we focus on the strong-intraspecies-coupling regime with fixed $g_{AA} = g_{BB} = 9$, while interspecies couplings, g_{AB} and g_{BA} , are chosen independently.

The last two continuum parameters cannot be directly obtained from particle parameters. Yet, as explained in [3], the velocity reduction parameter, ζ , can be determined from pair correlation functions. For the chosen Péclet number and area fraction, one obtains $z = \zeta \rho_0^a \tau / \ell = 57.63 \rho_0^a \tau / \ell = 0.37 \text{Pe} / \rho_0^{\text{con}}$ with $\rho_0^{\text{con}} = 1$. Further, we choose $D_t = 9$ in our continuum description [3].

IV. FIELD-THEORETICAL RESULTS

In this section, we provide details on the results obtained from the continuum model introduced in Sec. III.

A. Mean-field linear stability analysis around (anti)flocking base states

Linear stability analyses are analytical tools used to predict large-scale collective behavior in continuum systems. For the system at hand, the decay or growth of perturbations to the disordered base state, defined as $\rho_b^a = 1$ and $\mathbf{w}_b^a = \mathbf{0}$, has been previously studied in [2, 3, 8]. These analyses predict the formation of polarized states, related to wavenumber $k = 0$ -perturbations, as well as clustering at $k > 0$.

In this study, we are additionally focus on the linear stability of the (anti)flocking state. For simplicity, we assume that the (anti)flocking base state is orientated along the x -direction. The base state is then defined as $\rho_b^a = 1$ and

$\mathbf{w}_b^a = (w_0^a, 0)^T$, where w_0^A and w_0^B may differ. A flocking (antiflocking) base state is characterized by $w_0^A w_0^B > (<)0$. Importantly, the constant base state needs to fulfill the (fixed point) continuum Eqs. (4)-(6).

We are interested in the time evolution of perturbations to these base states. If the perturbations decay over time, the considered base state is stable. On the other hand, growing perturbations indicate the instability of the base state. Unlike the isotropic disordered base state considered in previous works [2, 3, 8], the (anti)flocking base states are anisotropic. Thus, we need to distinguish between perturbations along the direction of the base state (longitudinal) and transversal to it. In the main text, we focus on $k = 0$ -perturbations. In Sec. IV D of this Supplemental Material, we consider also the case of arbitrary \mathbf{k} .

We consider perturbations

$$\delta\rho^a(\mathbf{r}, t) = \int \hat{\rho}^a(\mathbf{k}) e^{i\mathbf{k}\cdot\mathbf{r} + \sigma(\mathbf{k})t} d\mathbf{k} \quad (9a)$$

$$\delta\mathbf{w}^a(\mathbf{r}, t) = \int \hat{\mathbf{w}}^a(\mathbf{k}) e^{i\mathbf{k}\cdot\mathbf{r} + \sigma(\mathbf{k})t} d\mathbf{k}, \quad (9b)$$

expressed as plane waves with complex growth rates $\sigma(\mathbf{k})$ and amplitudes $\hat{\rho}^a(\mathbf{k})$ and $\hat{\mathbf{w}}^a(\mathbf{k})$. The perturbations (9) involve all wave vectors \mathbf{k} . The growth rate σ depends on the magnitude and direction of \mathbf{k} .

We then insert $\rho^a = \rho_b + \delta\rho^a$ and $\mathbf{w}^a = \mathbf{w}_b^a + \delta\mathbf{w}^a = (w_0^a, 0)^T + \delta\mathbf{w}^a$ into the time evolution Eqs. (4)-(6) and neglect perturbations of order δ^2 . Note that the (constant) terms cancel since the base state is a fixed point.

The resulting linearized time-evolution equation for perturbations to the density of species A (for arbitrary \mathbf{k}) is given by

$$\begin{aligned} \partial_t \delta\rho^A &= \delta\rho^A \left[-D_t k^2 + z w_0^A i k_x \right] + \delta\rho^B \left[z w_0^A i k_x \right] + \delta w_x^A \left[-i k_x v^{\text{eff}}(\rho_0) \right] + \delta w_y^A \left[-i k_y v^{\text{eff}}(\rho_0) \right] \\ &=: A_{\rho^A}^{\rho^A} \delta\rho^A + A_{\rho^A}^{\rho^B} \delta\rho^B + A_{\rho^A}^{w_x^A} \delta w_x^A + A_{\rho^A}^{w_y^A} \delta w_y^A + A_{\rho^A}^{w_x^B} \delta w_x^B + A_{\rho^A}^{w_y^B} \delta w_y^B. \end{aligned} \quad (10)$$

The polarization can be perturbed either along or transversal to the direction of the base state. For polarizations perturbations along the base state, i.e., in x -direction, the time-evolution equation for species A reads

$$\partial_t \delta w_x^A = A_{w_x^A}^{\rho^A} \delta\rho^A + A_{w_x^A}^{\rho^B} \delta\rho^B + A_{w_x^A}^{w_x^A} \delta w_x^A + A_{w_x^A}^{w_y^A} \delta w_y^A + A_{w_x^A}^{w_x^B} \delta w_x^B + A_{w_x^A}^{w_y^B} \delta w_y^B. \quad (11)$$

with

$$A_{w_x^A}^{\rho^A} = -\frac{1}{2} i k_x (v^{\text{eff}}(\rho_0) - z \rho_0^a) + g'_{AA} w_0^A + g'_{AB} w_0^B + z w_0^A k^2 + \frac{g'_{AA}}{8 D_r} (w_0^A)^2 i k_x z + \frac{g'_{AB}}{8 D_r} w_0^A w_0^B i k_x z, \quad (12)$$

$$A_{w_x^A}^{\rho^B} = \frac{1}{2} i k_x z \rho_0^a + z w_0^A k^2 + \frac{g'_{AA}}{8 D_r} (w_0^A)^2 i k_x z + \frac{g'_{AB}}{8 D_r} w_0^A w_0^B i k_x z, \quad (13)$$

$$\begin{aligned} A_{w_x^A}^{w_x^A} &= -D_r + g'_{AA} \rho_0^A - D_t k^2 - \frac{(v^{\text{eff}}(\rho_0))^2}{16 D_r} k^2 - \frac{g'_{AA}}{2 D_r} 3 (w_0^A)^2 - \frac{g'_{AB}}{2 D_r} (w_0^B)^2 - \frac{g'_{AA} g'_{AB}}{D_r} 2 w_0^A w_0^B \\ &+ \frac{g'_{AA}}{8 D_r} \{ -3 w_0^A i k_x v^{\text{eff}}(\rho_0) \} + \frac{g'_{AB}}{8 D_r} \{ -w_0^B i k_x v^{\text{eff}}(\rho_0) \}, \end{aligned} \quad (14)$$

$$A_{w_x^A}^{w_y^A} = \frac{g'_{AA}}{8 D_r} \{ -5 w_0^A i k_y v^{\text{eff}}(\rho_0) \} + \frac{g'_{AB}}{8 D_r} \{ -3 w_0^B i k_y v^{\text{eff}}(\rho_0) \}, \quad (15)$$

$$A_{w_x^A}^{w_x^B} = g'_{AB} \rho_0^A - \frac{g'_{AA} g'_{AB}}{D_r} (w_0^A)^2 - \frac{g'_{AB}}{2 D_r} 2 w_0^A w_0^B + \frac{g'_{AB}}{8 D_r} \{ -2 w_0^A i k_x v^{\text{eff}}(\rho_0) \}, \quad (16)$$

and

$$A_{w_x^A}^{w_y^B} = \frac{g'_{AB}}{8 D_r} \{ -2 w_0^A i k_y v^{\text{eff}}(\rho_0) \}. \quad (17)$$

For polarization perturbations in y -direction, one obtains

$$\partial_t \delta w_y^A = A_{w_y^A}^{\rho^A} \delta\rho^A + A_{w_y^A}^{\rho^B} \delta\rho^B + A_{w_y^A}^{w_x^A} \delta w_x^A + A_{w_y^A}^{w_y^A} \delta w_y^A + A_{w_y^A}^{w_x^B} \delta w_x^B + A_{w_y^A}^{w_y^B} \delta w_y^B. \quad (18)$$

with

$$A_{w_y^A}^{\rho^A} = -\frac{1}{2} i k_y (v^{\text{eff}}(\rho_0) - z \rho_0^a) + \frac{g'_{AA}}{8 D_r} (-3 (w_0^A)^2) i k_y z + \frac{g'_{AB}}{8 D_r} (-3 w_0^A w_0^B) i k_y z, \quad (19)$$

$$A_{w_y^A}^{\rho^B} = \frac{1}{2} i k_y z \rho_0^a + \frac{g'_{AA}}{8 D_r} (-3 (w_0^A)^2) i k_y z + \frac{g'_{AB}}{8 D_r} (-3 w_0^A w_0^B) i k_y z, \quad (20)$$

$$A_{w_y^A}^{w_x^A} = \frac{g'_{AA}}{8 D_r} \{5 w_0^A i k_y v^{\text{eff}}(\rho_0)\} + \frac{g'_{AB}}{8 D_r} \{3 w_0^B i k_y v^{\text{eff}}(\rho_0)\}, \quad (21)$$

$$A_{w_y^A}^{w_y^A} = -D_r + g'_{AA} \rho_0^A - D_t k^2 - \frac{(v^{\text{eff}}(\rho_0))^2}{16 D_r} k^2 - \frac{g'_{AA}}{2 D_r} (w_0^A)^2 - \frac{g'_{AB}}{2 D_r} (w_0^B)^2 - \frac{g'_{AA} g'_{AB}}{D_r} w_0^A w_0^B \\ + \frac{g'_{AA}}{8 D_r} \{-3 w_0^A i k_x v^{\text{eff}}(\rho_0)\} + \frac{g'_{AB}}{8 D_r} \{-w_0^B i k_x v^{\text{eff}}(\rho_0)\}, \quad (22)$$

$$A_{w_y^A}^{w_x^B} = \frac{g'_{AB}}{8 D_r} \{2 w_0^A i k_y v^{\text{eff}}(\rho_0)\}, \quad (23)$$

and

$$A_{w_y^A}^{w_y^B} = g'_{AB} \rho_0^A + \frac{g'_{AB}}{8 D_r} \{-2 w_0^A i k_x v^{\text{eff}}(\rho_0)\}. \quad (24)$$

The equations for species B are obtained by exchanging $A \leftrightarrow B$.

To analyze the results, we consider perturbations in a different basis, that is, $\delta\rho^A \pm \delta\rho^B$ and $\delta\mathbf{w}^A \pm \delta\mathbf{w}^B$. These can be easily obtained by rewriting

$$\delta\rho^A = \frac{1}{2} ((\delta\rho^A + \delta\rho^B) + (\delta\rho^A - \delta\rho^B)) \quad (25)$$

and

$$\delta\rho^B = \frac{1}{2} ((\delta\rho^A + \delta\rho^B) - (\delta\rho^A - \delta\rho^B)). \quad (26)$$

The time evolution of $\delta\rho^A \pm \delta\rho^B$ is then given by

$$2 \partial_t (\delta\rho^A \pm \delta\rho^B) = (\delta\rho^A + \delta\rho^B) ((A_{\rho^A}^{\rho^A} \pm A_{\rho^B}^{\rho^A}) + (A_{\rho^A}^{\rho^B} \pm A_{\rho^B}^{\rho^B})) \\ + (\delta\rho^A - \delta\rho^B) ((A_{\rho^A}^{\rho^A} \pm A_{\rho^B}^{\rho^A}) - (A_{\rho^A}^{\rho^B} \pm A_{\rho^B}^{\rho^B})) \\ + (\delta w_x^A + \delta w_x^B) ((A_{\rho^A}^{w_x^A} \pm A_{\rho^B}^{w_x^A}) + (A_{\rho^A}^{w_x^B} \pm A_{\rho^B}^{w_x^B})) \\ + \text{other contributions from } (\delta\mathbf{w}^A \pm \delta\mathbf{w}^B). \quad (27)$$

For $\delta\mathbf{w}^A \pm \delta\mathbf{w}^B$, the expressions can be obtained equivalently.

B. Characterization of emerging states

The emerging non-equilibrium states can be characterized in terms of eigenvalues and the eigenvector corresponding to the largest real eigenvalue.

For the disordered base state, the characterization follows the more detailed explanations in [2, 3, 8]. The most important points are the following: Instabilities at wave number $k = 0$ pertain to flocking or antiflocking instabilities. The eigenvector corresponding to the largest (real) growth rate then indicates whether flocking (in $(\mathbf{w}^A + \mathbf{w}^B)$ -direction) or antiflocking (in $(\mathbf{w}^A - \mathbf{w}^B)$ -direction) is predicted. At $k > 0$, phase separation behavior comes into play. If the maximum growth rate is found at a finite $k > 0$, phase separation is predicted. Phase separation can occur alone or in combination with flocking. We use the angle between perturbations of total density ($\rho^A + \rho^B$) and composition ($\rho^A - \rho^B$) at small k to predict the type of phase separation. Both species can cluster symmetrically, demix or partially demix in form of asymmetric clustering of predominately one species. Imaginary growth rates with positive real parts indicate oscillatory instabilities, which are generally related to non-stationary behavior.

In the main text, we focus on the stability of base states against $k = 0$ -perturbations and the appearance exceptional points (which appear only at $k = 0$, see Sec. IV C). The case of arbitrary \mathbf{k} is considered in Sec. IV D in this Supplemental Material.

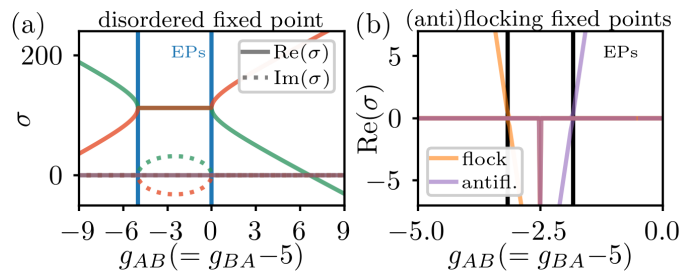


FIG. 6. Growth rates at $k = 0$ and exceptional points of the (a) disordered and (b) flocking and antiflocking base states for $g_{AB} = g_{BA} - 5$ and $R_\theta = 10\ell$. Exceptional points (EPs) are indicated as vertical lines. The six eigenvalues of the disordered base state are all colored differently. The six eigenvalues of the flocking (antiflocking) base state are all colored in orange (purple). Other parameters are as specified in Appendix III C.

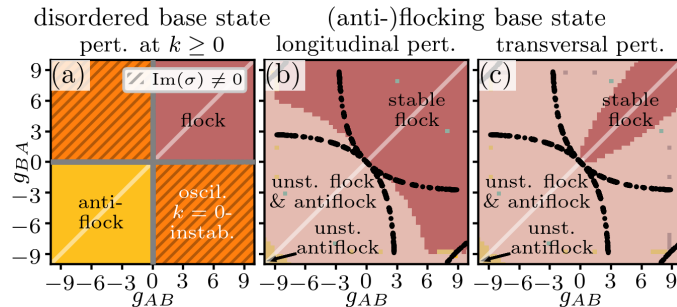


FIG. 7. Stability diagrams for arbitrary $k \geq 0$ -instabilities. The diagrams are obtained from linear stability analyses of the (a) isotropic disordered and (b,c) homogeneous (anti)flocking base states of the continuum Eqs. (4)-(6). Perturbations to the (anti)flocking base states can be (b) longitudinal or (c) transversal to the base state. Exceptional points of the disordered and (anti)flocking base states are indicated as gray and black lines, respectively. The alignment radius is $R_\theta = 10\ell$. Other parameters are specified in Sec. III C.

C. Exceptional points

Exceptional points have been related to parity-time symmetry breaking transitions in nonreciprocal scalar [10, 11] and polar active systems [9]. They are defined as points where eigenvalues of a linear stability matrix coalesce and eigenvectors become parallel [12]. When exceptional points coincide with a bifurcation, a point where a qualitative change in the system's behavior takes place, the exceptional point is referred to as “critical exceptional point” [13].

Our system features three homogeneous base states. These are the disordered, flocking, and antiflocking base states. The growth rates of $k = 0$ -perturbations to these base states and corresponding exceptional points are shown for nonreciprocal systems with $g_{AB} = g_{BA} - d$ in Fig. 6.

We can make the following observations. Exceptional points only occur at wave number $k = 0$. Starting from the disordered base state [Fig. 6(a)], exceptional points have a positive real growth rate, $\text{Re}(\sigma^{\text{dis}}) > 0$. Two pairs of eigenvalues meet at $g_{AB} = 0$ and $g_{AB} = -d$, where we obtain two sets of two parallel eigenvectors. Between the exceptional points, the growth rates becomes imaginary.

For the flocking and antiflocking base states [Figs. 6(b)], exceptional points occur in combination with bifurcations, i.e., the largest real growth rates are $\text{Re}(\sigma^{\text{fl}}) = \text{Re}(\sigma^{\text{antifl}}) = 0$. Thus, these exceptional points are critical exceptional points. The imaginary part of the growth rate is zero at all g_{AB} . Both, flocking and antiflocking base states are stable between the exceptional points ($\text{Re}(\sigma^{\text{fl}}), \text{Re}(\sigma^{\text{antifl}}) \leq 0$). Then, at the exceptional point, either flocking or antiflocking becomes unstable with at least one $\text{Re}(\sigma^{\text{fl/antifl}}) > 0$.

D. Results for finite-wavelength perturbations

Finite-wavelength perturbations (with $k > 0$) provide further insights into the details of collective behavior.

The non-equilibrium phase diagram for perturbations of arbitrary $k \geq 0$ is shown in Fig. 7. The stability of the disordered base state [Fig. 7(a)] is identical for $k \geq 0$ and $k = 0$. This indicates that the instabilities of the

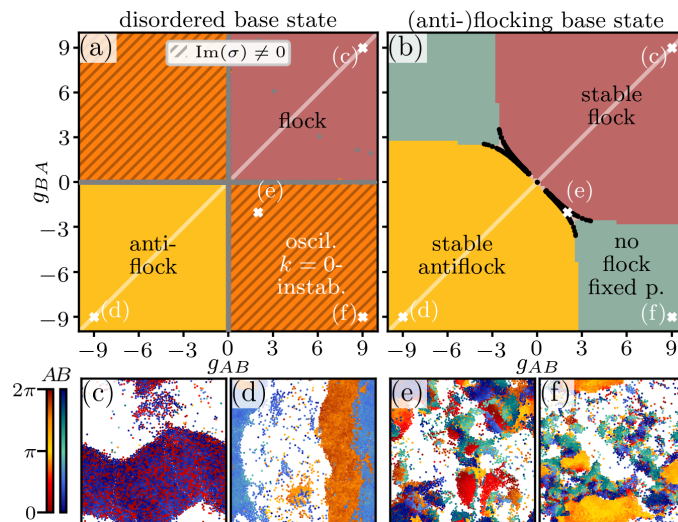


FIG. 8. Stability diagrams at $k = 0$ and particle simulation snapshots for alignment radius $R_\theta = 2\ell$. The stability diagrams are obtained from linear stability analyses of the (a) uniform disordered and (b) homogeneous (anti)flocking base states of the $k = 0$ -continuum Eq. (7). Exceptional points of the disordered and (anti)flocking base states are indicated as gray and black lines, respectively. BD simulation snapshots at (c) $g_{AB} = g_{BA} = 9$, (d) $g_{AB} = g_{BA} = -9$, (e) $g_{AB} = -g_{BA} = 2$, and (f) $g_{AB} = -g_{BA} = 9$. Other parameters are specified in Sec. III C.

disordered state are dominated by $k = 0$ -instabilities, which are related to polarization dynamics. We note that, for smaller alignment radii and thus reduced effective interactions, additional (a)symmetric clustering instabilities arise, see Sec. V.

The stability of the flocking and antiflocking states against longitudinal and transversal $k \geq 0$ -perturbations is shown in Figs. 7(b,c). Homogeneous flocking states are only stable when interspecies alignment is nearly reciprocal, i.e., $g_{AB} \approx g_{BA} > 0$. Homogeneous antiflocking, on the other hand, is unstable across all interspecies coupling strengths, including, in particular, $g_{AB} \approx g_{BA} < 0$.

These continuum predictions are consistent with the particle simulation results shown in the snapshots in Fig. 1(c,d) in the main text. The reciprocal flocking state [Fig. 1(c)] exhibits a nearly homogeneous density distribution, while the reciprocal antiflocking state [Fig. 1(d)] is characterized by unstable, bending bands.

V. SMALLER ALIGNMENT RADIUS: CONTINUUM VERSUS PARTICLE SCALE

In the main text, we focus on a system with relatively large radius of alignment interactions, $R_\theta = 10\ell$. Here, we show that also at smaller alignment radii, spontaneous chirality emerges due to nonreciprocal couplings. However, reducing the interaction radius decreases the “effective” alignment strength, which scales as $g'_{ab} \sim R_\theta^2$ on the continuum level. This reduction has consequences on both the continuum and particle levels, which we address in the following.

On the continuum level, there are indeed distinct differences in the predicted non-equilibrium behavior when we consider smaller R_θ , e.g., $R_\theta = 2\ell$. The corresponding non-equilibrium phase diagrams for $k = 0$ and $k \geq 0$ are shown in Figs. 8 and 9, respectively. The disordered base state [Fig. 8(a)] exhibits stationary flocking and antiflocking ($k = 0$ -)instabilities, as well as oscillatory $k = 0$ -instabilities when species have opposite alignment goals ($g_{AB} g_{BA} < 0$), exactly like for larger R_θ . However, finite-wavelength perturbations with $k > 0$ [Fig. 9(a)] predict additional clustering instabilities, which are suppressed for larger R_θ [Fig. 7(a)]. The phenomenon of nonreciprocity-induced asymmetric clustering and its origin is discussed in [2, 3]. The predicted clustering instabilities qualitatively agree with particle simulation results, where snapshots [Figs. 8(e,f)] show the formation of single-species clusters of species A for $g_{AB} = -g_{BA} = \delta > 0$.

Perturbations to the (anti)flocking base states reveal differences compared to larger R_θ already at $k = 0$, see Fig. 8(b). When species have strongly opposing alignment goals, neither flocking nor antiflocking states are fixed point solutions to the continuum Eq. (7). The regimes of stable flocking and antiflocking are separated from the regimes without (anti)flocking fixed points by exceptional points [black dots in Figs. 8(a,b)]. For $k \geq 0$, the non-equilibrium phase diagrams at $R_\theta = 2\ell$ for longitudinal and transversal perturbations are shown in Figs. 9(b,c). The antiflocking base state is unstable to both types of perturbations, whereas the flocking base state is stable against longitudinal but unstable to transversal ones.

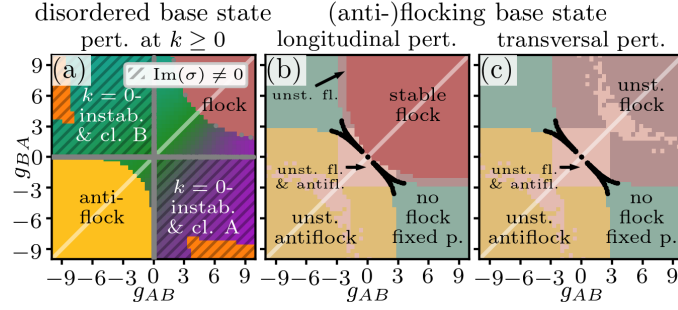


FIG. 9. Stability diagrams for arbitrary $k \geq 0$ -instabilities for alignment radius $R_\theta = 2\ell$. The stability diagrams are obtained from linear stability analyses of the (a) isotropic disordered and (b,c) homogeneous (anti)flocking base states of the continuum Eqs. (4)-(6). Perturbations to the (anti)flocking base states can be (b) longitudinal and (c) transversal to the direction of the base state. Exceptional points of the disordered and (anti)flocking base states are indicated as gray and black lines, respectively. Other parameters are specified in Sec. III C.

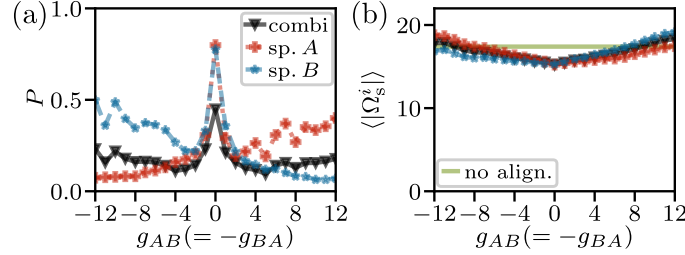


FIG. 10. Polarization and spontaneous chirality for antisymmetric system with $g_{AB} = -g_{BA}$ and $R_\theta = 2\ell$.

These continuum theory results conform with particle simulations, as seen in the snapshots in Figs. 8(c,d). At large $g_{AB}, g_{BA} > 0$, flocking is predicted and highly polarized bands are observed at the particle level. The formation of these bands confirms the flocking state's stability against longitudinal and instability against transversal perturbations. In contrast, the bands in the antiflocking state at large $g_{AB}, g_{BA} < 0$ are more dynamic, reflecting the instability against both longitudinal and transversal perturbations.

To quantitatively analyze the effect of nonreciprocity at smaller alignment radii, we examine the time- and noise-averaged polarization and spontaneous chirality for antisymmetric couplings in Fig. 10 and for cases crossing exceptional points in Fig. 11.

In systems with antisymmetric couplings, $g_{AB} = -g_{BA} = \delta$, the combined polarization remains small ($P_{\text{combi}} < 0.3$) for all non-zero δ [Fig. 10(a)]. As seen in the snapshot in Fig. 8(e), weak nonreciprocity ($\delta = 2$) leads to the formation of many small single-species clusters, predominantly of the more aligning species *A*. Thus, for small $\delta > 0$, $P_A > P_B$. This behavior contrasts with systems with $R_\theta = 10\ell$. There, weak nonreciprocity produces one large polarized cluster for both species each. The antialigning particles trap some aligning particles inside their cluster, leading to $P_B > P_A$ for small $\delta > 0$ [Fig. 1(e) in the main text]. At larger nonreciprocity [$\delta = 9$, Figs. 1(f) in the main text and 8(f) in this Supplemental Material], large polarized single-species clusters form regardless of the alignment radius, leading to $P_A > P_B$ for $\delta > 0$. The nonreciprocity-induced spontaneous chirality at $R_\theta = 2\ell$ [Fig. 10(b)], increases with increasing strength $|\delta|$ of nonreciprocity, but remains below the noise-induced chirality for $|\delta| < 9$. Only at higher $\delta \geq 9$, it exceeds the noise-induced chirality.

To summarize, the nonreciprocity-induced chirality is weaker for $R_\theta = 2\ell$ compared to $R_\theta = 10\ell$, but it remains measurable. However, the signatures of exceptional points become less prominent for $R_\theta = 2\ell$. In oscillatory instability regime, the polarization increases with increasing $g_{AB} = (g_{BA} - 5)$ [Fig. 11(a)], but clear peaks in the spontaneous chirality near the critical exceptional points are not observed [Fig. 11(b)].

In the main text we therefore focus on the larger coupling radius, $R_\theta = 10\ell$, where effective interactions between particles are stronger and the effects of nonreciprocity are more pronounced.

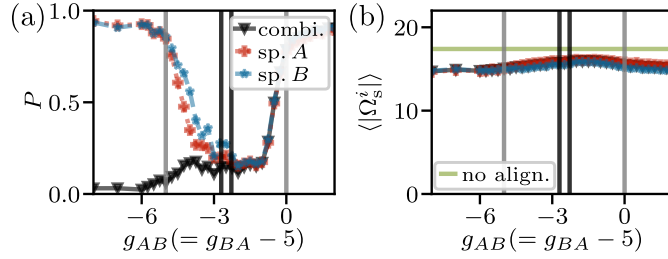


FIG. 11. Polarization and spontaneous chirality for antisymmetric system with $g_{AB} = g_{BA} - 5$ and $R_\theta = 2\ell$. Exceptional points of the disordered and (anti)flocking base states are indicated as gray and black vertical lines, respectively.

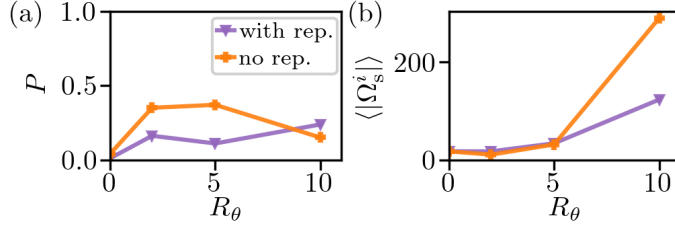


FIG. 12. Polarization and mean absolute value of spontaneous chirality as a function of alignment radius R_θ for antisymmetric system with $g_{AB} = -g_{BA} = 9$. The average to calculate P and $\langle |\Omega_s^i| \rangle$ is taken over all particles.

VI. EFFECT OF REPULSION ON THE PARTICLE SCALE

All results in the main text pertain to systems with steric repulsion and a large interaction radius ($R_\theta = 10\ell$). Importantly, nonreciprocity-induced chirality is also present in systems without repulsion, as well as in those with smaller interaction radii, see Sec. V. However, the precise interplay of repulsion and alignment radius on the dynamical behavior at the particle level is non-trivial.

As an example, we consider in Fig. 12, the dependency of overall polarization and the spontaneous chirality on R_θ for $\delta = 9$. We see that they differ between systems with and without repulsion.

For systems with repulsion, the polarization remains approximately constant for all R_θ due to nearly R_θ -independent asymmetric cluster formation with highly polarized single-species particles [purple line in Fig. 12(a), snapshots in Fig. 1(f) of the main text and Fig. 8(f) of the Supplemental Material]. Chiral motion, on the other hand, is induced by nonreciprocal couplings with particles of the other species. Thus, it increases with increasing R_θ due to enhanced chances of having opposite-species particles within the interaction radius.

In contrast, for systems without repulsion (orange line), the polarization first increases for intermediate radii ($R_\theta \lesssim 5\ell$), but then decreases again for larger $R_\theta (= 10\ell)$. The reason is that, when the interaction radius is relatively small, non-repulsive particles of the same species cluster in very small regions. Within these single-species cluster, particles strongly align their motion, which leads to a large polarization. However, at the same time, it becomes unlikely that two tightly accumulated single-species clusters are close enough to interact within the small interaction radius. This limits the occurrence of nonreciprocal interspecies couplings and results in low spontaneous chirality. Yet, with larger coupling radii, particles become more easily influenced by particles of the opposite species, and single-species clustering occurs less. While this leads to decreased polarization, nonreciprocal couplings are increased. The resulting nonreciprocity-induced spontaneous chirality is very large since nonrepulsive particles can move freely without being hindered by other particles.

Thus, the particle behavior is crucially affected by the non-trivial interplay of intraspecies alignment couplings, which tend to drive single-species accumulations [3, 14, 15], and the number of interacting neighbors, which depends on the alignment radius.

VII. LIST OF SUPPLEMENTARY VIDEOS

To visualize the spontaneous chirality in nonreciprocal polar active mixtures, we provide BD simulation videos for the following cases:

- antisymmetric couplings with moderate nonreciprocity: $g_{AB} = -g_{BA} = -2.5$,

- antisymmetric couplings with strong nonreciprocity: $g_{AB} = -g_{BA} = 9$,
- coupling parameters close to a critical exceptional point: $g_{AB} = g_{BA} - 5 = -3$.

The videos show exemplary non-equilibrium steady states for a single random initial configuration. The parameters are chosen as described in Sec. I.

-
- [1] J. D. Weeks, D. Chandler, and H. C. Andersen, Role of repulsive forces in determining the equilibrium structure of simple liquids, *J. Chem. Phys.* **54**, 5237 (1971).
- [2] K. L. Kreienkamp and S. H. L. Klapp, Non-reciprocal alignment induces asymmetric clustering in active mixtures, arXiv preprint arXiv:2403.19291 (To appear in *Phys. Rev. Lett.*) (2024).
- [3] K. L. Kreienkamp and S. H. L. Klapp, Non-reciprocal alignment induces asymmetric clustering in active mixtures, arXiv preprint arXiv:2404.06305 (To appear in *Phys. Rev. E*) (2024).
- [4] J. Chen, X. Lei, Y. Xiang, M. Duan, X. Peng, and H. Zhang, Emergent chirality and hyperuniformity in an active mixture with nonreciprocal interactions, *Phys. Rev. Lett.* **132**, 118301 (2024).
- [5] G. Baglietto and E. V. Albano, Finite-size scaling analysis and dynamic study of the critical behavior of a model for the collective displacement of self-driven individuals, *Phys. Rev. E* **78**, 021125 (2008).
- [6] A. Cavagna, I. Giardina, and T. S. Grigera, The physics of flocking: Correlation as a compass from experiments to theory, *Physics Reports* **728**, 1 (2018).
- [7] J. Bartnick, M. Heinen, A. V. Ivlev, and H. Löwen, Structural correlations in diffusiophoretic colloidal mixtures with nonreciprocal interactions, *J. Condens. Matter Phys.* **28**, 025102 (2015).
- [8] K. L. Kreienkamp and S. H. L. Klapp, Clustering and flocking of repulsive chiral active particles with non-reciprocal couplings, *New J. Phys.* **24**, 123009 (2022).
- [9] M. Fruchart, R. Hanai, P. B. Littlewood, and V. Vitelli, Non-reciprocal phase transitions, *Nature* **592**, 363 (2021).
- [10] Z. You, A. Baskaran, and M. C. Marchetti, Nonreciprocity as a generic route to traveling states, *Proc. Natl. Acad. Sci. U.S.A.* **117**, 19767 (2020).
- [11] T. Suchanek, K. Kroy, and S. A. M. Loos, Irreversible mesoscale fluctuations herald the emergence of dynamical phases, *Phys. Rev. Lett.* **131**, 258302 (2023).
- [12] R. El-Ganainy, K. G. Makris, M. Khajavikhan, Z. H. Musslimani, S. Rotter, and D. N. Christodoulides, Non-Hermitian physics and PT symmetry, *Nat. Phys.* **14**, 11 (2018).
- [13] T. Suchanek, K. Kroy, and S. A. Loos, Entropy production in the nonreciprocal Cahn-Hilliard model, *Phys. Rev. E* **108**, 064610 (2023).
- [14] T. Vicsek, A. Czirók, E. Ben-Jacob, I. Cohen, and O. Shochet, Novel type of phase transition in a system of self-driven particles, *Phys. Rev. Lett.* **75**, 1226 (1995).
- [15] E. Sesé-Sansa, I. Pagonabarraga, and D. Levis, Velocity alignment promotes motility-induced phase separation, *EPL* **124**, 30004 (2018).